System Identification and Handling Qualities Predictions of an eVTOL Urban Air Mobility Aircraft Using Modern Flight Control Methods

Robert Niemiec

Research Scientist

Farhan Gandhi

Redfern Professor
and MOVE Director

Mark J. S. Lopez

Aerospace Engineer

Mark B. Tischler

Senior Scientist

Center for Mobility With Vertical Lift
Rensselaer Polytechnic Institute
Troy, NY, United States

U.S. Army Combat Capabilities Development
Command Aviation & Missile Center
Moffet Field, CA, United States

ABSTRACT

Modern system identification techniques were used to identify a linear model based on a nonlinear simulation of a concept Urban Air Mobility quadcopter, and compared to a perturbation-based model. These models were used to develop feedback controllers for both variable-pitch and variable-RPM variants of the quadcopter, with the handling qualities requirements determining current requirements for the electric motors. To have sufficient stability margins and bandwidth, the motor time constant for the variable-RPM system must be no greater than 0.122s. Both variable-RPM and variable-pitch systems were limited by the yaw axis, which relies on differential motor torque for control. The introduction of rotor cant alleviated this problem for the variable-pitch vehicle, allowing a 47% reduction in motor weight, relative to the uncanted variable-pitch system.

NOTATION

A	Matrix of stability derivatives
$\bar{A}$	Reduced matrix of stability derivatives
B	Matrix of control derivatives
$\bar{B}$	Reduced matrix of control derivatives
I_{motor}	Motor Inertia
I_{rotor}	Rotor Inertia
i	Motor Current
K_e	Motor Back EMF Constant
K_t	Motor Torque Constant
L	Motor Inductance
Q_A	Aerodynamic Torque
R_m	Motor Internal Resistance
r	Transmission Gear Ratio
u	Vehicle control inputs
V	Motor Voltage
x	Vehicle states
Ψ	Azimuthal Rotor Location
Ω	Rotor Rotational Speed

Subscripts

f	Fuselage
r	Rotor
m	Motor
hov	Hover Trim Value

Multirotor Control Subscripts

0	Collective
1s	Lateral
1c	Longitudinal
0d	Differential (Yaw)

INTRODUCTION

Interest in electric Vertical Takeoff and Landing (eVTOL) for Urban Air Mobility (UAM), driven by low barriers to entry, has grown dramatically in recent years. Numerous designs have emerged not only from established VTOL manufacturers, such as Bell and Airbus Helicopters, but from new entrants to the VTOL space, including Joby Aviation and the Hyundai Motor Company, among many others. The flexibility of electric power distribution has allowed numerous different designs, ranging from scaled-up multicopters (such as the Volocopter 2X or Airbus CityAirbus), to tiltrotors (Bell Nexus and A[3] Vahana), to entirely new archetypes (such as the Wisk Cora or Aurora Flight Sciences Pegasus Passenger Air Vehicle).

One challenge in developing flight control systems for these eVTOLs is the development of a flight-accurate dynamics model. System identification techniques produce linear state-space models of real aircraft by using real-world test data to estimate stability and control derivatives. These techniques have been used on conventional VTOL aircraft for decades (Ref. 1), and have been applied to small-scale multicopters as well. Wei (Ref. 2) and Ivler (Ref. 3) used the frequency domain system ID suite CIFER® (Ref. 4) to generate linear models of a quadcopter and hexacopter, respectively. The

U.S. Army Combat Capabilities Development Aviation and Missile Center has also conducted a great deal of work on system identification and controller optimization on the IRIS+ quadcopter (Ref. 5), including minimizing position response to turbulence inputs.

The handling qualities metrics defined in ADS-33 (Ref. 6) have been applied to multicopters at different scales. In Ref. 7, Ivler et. al apply Froude scaling based on the maximum velocity of the IRIS+ quadcopter relative to the UH-60, to obtain scaled requirements for the unmanned vehicle. In Ref. 8, Ivler et. al apply Froude scaling based on the hub-to-hub diameter of a hexacopter. Walter et. al (Ref. 9) also applied this type of Froude-scaling to quadcopters across several sizes, showing that motor limitations made it impossible to satisfy the scaled requirements without saturating the motors for even mild commands in roll.

Malpica and Withrow-Maser (Ref. 10) conducted a study into variable-pitch and variable-RPM variants of 1- to 6-passenger NASA concept quadcopters (Ref. 11). While Malpica and Withrow-Maser found that the variable-pitch vehicles were capable of satisfying ADS-33 handling qualities requirements, the limitations of their drive system (which severely limited the torque provided for rotor acceleration) prevented stabilization of the variable-RPM variants. This result held across all of their scales, which ranged from a 1,200 lb vehicle with 6.5ft radius rotors to a 5700lb vehicle with 12.3ft radius rotors.

Similar to Ref. 10, the objective of the present study is to analyze variable-pitch and variable-RPM variants of the 1-passenger NASA Concept Quadcopter using modern flight control methods. However, rather than identifying a drive system limit, and attempting to design a controller that stabilizes the vehicle subject to that limit, the current study will optimize the control system for controller effort, ignoring drive system limitations, and use that result to identify the *minimum requirement* for a variable-RPM system to be feasible at the UAM scale. These requirements will be identified for both the variable-RPM system and the variable-pitch system, and the requisite motor weight will be compared.

The system identification tool CIFER® (Ref. 4) will be used to identify linear models from a nonlinear dynamic simulation. The linear models will be used with the control optimization suite CONDUIT® (Ref. 12) to optimize linear controllers for both closed-loop and disturbance rejection. Several types of piloted inputs will be applied to the closed-loop system, and the motor commands used to stabilize the aircraft or follow trajectories will be used to determine the current and voltage requirements for the individual motors.

PLATFORM

The aircraft considered in this study is a single-passenger all-electric UAM quadcopter described in Refs. 10 and 13. The aircraft was sized using NDARC (NASA Design and Analysis of Rotorcraft) to carry a 250 lb payload, with a 2.5lb disk loading with a 50nm range. This resulted in a vehicle with specifications summarized in Table 1.

Table 1: NASA 1-Passenger Electric UAM Quadcopter Specifications

Parameter	Value
Gross Weight	5571 N (1252 lb)
Hub Separation (diagonal)	7.31 m (24 ft)
Rotor Radius (each)	1.92 m (6.31 ft)
Hover Tip Speed	137 m/s (450 ft/s)
Rotor Solidity	0.0646
Taper Ratio	0.75
Flapping Frequency	1.03/rev
Rotor Twist	-12°
δ_3	45°
Fuselage Flat Plate Drag Area	0.319 m^2 (3.43 ft^2)
Rotor	17.5 kg m^2 (12.9 slug ft^2)

The rotors are individually controlled with collective pitch only, not unlike a conventional helicopter's tail rotor. The rotors themselves are articulated, with 45° of δ_3 to reduce the flapping of the rotors in cruise (Ref. 13). Importantly, despite the inclusion of articulation in the rotors, the quadcopter does not rely on the flapping dynamics of the rotors to produce the aircraft-level moments, which are produced by differential thrust on the different rotors.

The rotors are assumed to be independently driven by dedicated motors in a direct-drive configuration. Therefore, each rotor has two controls associated with it: the collective pitch setting, and the motor voltage. The variable-pitch system primarily relies on the former to regulate the thrust of the rotor, while the latter is used to maintain a consistent rotor speed. On the variable-RPM system, the motor voltage is used to track a commanded rotor speed, which, in turn, regulates the forces and moments on the vehicle, while collective pitch is held constant.

MODEL AND ANALYSIS TOOLS

The Rensselaer Multicopter Analysis Code (RMAC, Ref. 14) is used as the basis of the analysis in this study. RMAC is a comprehensive analysis tool designed specifically for use on multicopters. RMAC calculates the rotor forces and moments using blade element theory coupled to a Peters-He finite state dynamic wake model.

The dynamic model takes as inputs the individual rotor collective pitch settings and motor voltages. The dynamic states include the traditional 6 degree of freedom (DOF) fuselage states (position, attitude, and linear and angular velocity), as well as flapping (6 per rotor) and inflow states (10 per rotor). In addition to these, the individual rotor speeds, Ω are included as vehicle states.

Motor Model

The brushless DC motor equations for the current and speed of a rotor are given by (Ref. 10):

$$(I_{\text{rotor}} + I_{\text{motor}} r^2)\dot{\Omega} = K_t r i - Q_A - B r^2 \Omega$$
$$Li = V - K_e r\Omega - R_m i \tag{1}$$

For a directly-driven rotor (no gearbox), $r = 1$. To simplify the equations, the current is assumed to settle instantaneously (essentially assuming that motor inductance L is very small, Ref. (Ref. 10)). With this assumption, and neglecting the viscous losses in the motor, as well as the motor's inertia (which is small compared to the rotational inertia of the rotor), Eq. 1 reduces to

$$I_{\text{rotor}}\dot{\Omega} = \frac{K_e}{R_m}V - \frac{K_e^2}{R_m}\Omega - Q_A \qquad (2)$$

which uses $K_e = K_t$, valid for SI units only. The motor parameters K_e and R_m are obtained using the method outlined in Ref. 10, assuming the same 95% efficiency in the motor. This results in a 1-state equation for each motor, which agrees with the flight-identified motor lag models for eVTOLs (Refs. 5, 15).

State Space Model

The evolution of the aircraft over time follows

$$\dot{x} = f(x, u) \qquad (3)$$

where x represents a concatenation of the states associated with the fuselage (x_f, 12 states–linear velocity, angular velocity, attitude, and position), rotors (x_r, 6 flapping states and 10 inflow states per rotor), and motors (x_m, 4 states, Ω_k). u represents the rotor collective pitches, and the motor voltages. Linearizing the results numerically yields a system of the form

$$\Delta\dot{x} = A\Delta x + B\Delta u \qquad (4)$$

Partitioning Eq. 4 into fuselage, rotor, and motor states yields

$$\begin{bmatrix} \Delta\dot{x}_f \\ \Delta\dot{x}_r \\ \Delta\dot{x}_m \end{bmatrix} = \begin{bmatrix} A_{ff} & A_{fr} & A_{fm} \\ A_{rf} & A_{rr} & A_{rm} \\ A_{mf} & A_{mr} & A_{mm} \end{bmatrix} \begin{bmatrix} \Delta x_f \\ \Delta x_r \\ \Delta x_m \end{bmatrix} + \begin{bmatrix} B_f \\ B_r \\ B_m \end{bmatrix}\Delta u \qquad (5)$$

The rotor flapping and inflow states are expected to evolve quickly compared to the fuselage and motor states, so the technique of static condensation is applied to reduce the system to the 16-state linear model

$$\begin{bmatrix} \Delta\dot{x}_f \\ \Delta\dot{x}_m \end{bmatrix} = \bar{A}\begin{bmatrix} \Delta x_f \\ \Delta x_m \end{bmatrix} + \bar{B}\Delta u \qquad (6)$$

where

$$\bar{A} = \begin{bmatrix} A_{ff} & A_{fm} \\ A_{mf} & A_{mm} \end{bmatrix} - \begin{bmatrix} A_{fr} \\ A_{mr} \end{bmatrix}A_{rr}^{-1}\begin{bmatrix} A_{rf} & A_{rm} \end{bmatrix}$$
$$\bar{B} = \begin{bmatrix} B_f \\ B_m \end{bmatrix} - \begin{bmatrix} A_{fr} \\ A_{mr} \end{bmatrix}A_{rr}^{-1}B_r \qquad (7)$$

For the variable-pitch system only, a perfect RPM-governor is assumed, such that $\Delta x_m \equiv 0$, and the rows and columns of $\bar{A}$ and $\bar{B}$ associated with Δx_m can be dropped (this also removes motor voltage from u). This results in a 12-state rigid body model, which can be reduced to a standard 8-state model by removing the position and heading states from Δx_f.

Control mixing is achieved using multi-rotor coordinates (Ref. 16), which for a quadcopter can be described by Eq. 8,
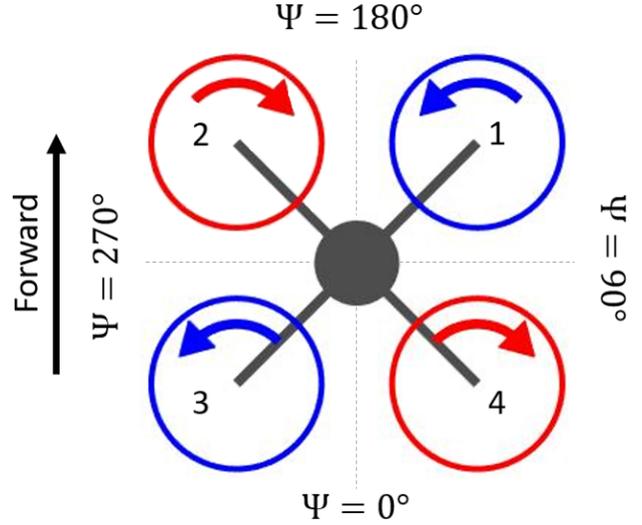

Figure 1: Quadcopter Configuration and Rotor Numbering

where the left-hand side represents the individual rotor collective pitches, and the right-hand side includes a vector representing the pilot inputs and a mixing matrix. The mixing matrix depends on a parameter Ψ_k which is an azimuthal coordinate defined as zero at the rear of the aircraft and increasing counter-clockwise as viewed from above (Fig. 1).

$$\begin{bmatrix} \theta_1 \\ \theta_2 \\ \theta_3 \\ \theta_4 \end{bmatrix} = \begin{bmatrix} 1 & \sin\Psi_1 & \cos\Psi_1 & 1 \\ 1 & \sin\Psi_2 & \cos\Psi_2 & -1 \\ 1 & \sin\Psi_3 & \cos\Psi_3 & 1 \\ 1 & \sin\Psi_4 & \cos\Psi_4 & -1 \end{bmatrix} \begin{bmatrix} \theta_0 \\ \theta_{1s} \\ \theta_{1c} \\ \theta_{0d} \end{bmatrix} \qquad (8)$$

θ_0 thus represents a mean rotor collective, and is used to regulate the heave dynamics of the vehicle. θ_{1s} increases collective pitch of rotors on the right side of the vehicle, while decreasing it on the left side, thus producing a roll-left moment. Similarly θ_{1c} produces a nose-down moment by enforcing a longitudinal differential collective pitch. Finally, θ_{0d} produces a nose-right moment by increasing the pitch on counter-clockwise spinning rotors, while decreasing the pitch on clockwise spinning rotors. This transform can be used on any parameter that can be associated with the individual rotors, and is also used to mix motor voltage inputs on the variable-RPM system. Conversely, multiplying individual motor parameters (such as current or Ω) by the inverse of this matrix will express them in axis-aligned coordinates.

System identification provides an additional way to obtain a linear model from the nonlinear simulation and assess the accuracy of the LTI model determined by numerical perturbation. In lieu of flight test data, control inputs to the full nonlinear model are swept, and the evolution of the model during the simulation is saved. Figure 2 shows one of these simulations, where the heave axis is excited by θ_0. Due to the symmetry of the quadcopter in hover, the vertical, longitudinal, lateral, and directional dynamics are all decoupled from one another.

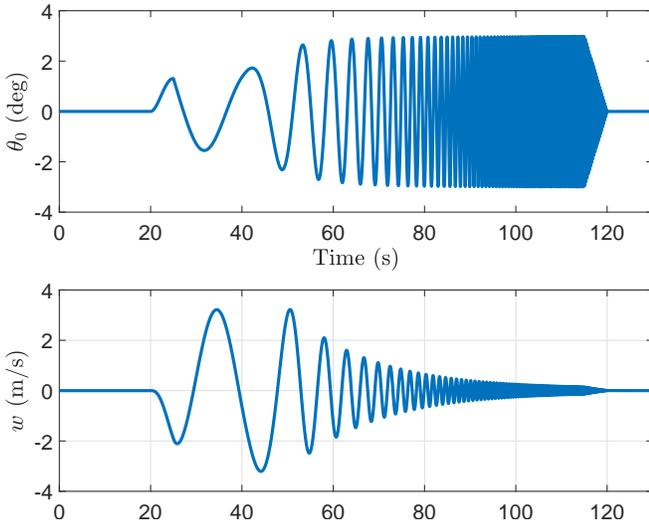The CIFER® system ID tool (Ref. 4) is used to generate frequency responses from the nonlinear simulation data, to

Figure 2: Heave Input Sweep

Figure 3: Heave Frequency Response

which low-order equivalent systems (LOES) can be identified, as shown in Fig. 3, which shows the frequency response generated from the time history data in Fig. 2. As expected, the data is very well-represented by a first-order transfer function, with a cost of $J = 14.28$, indicating that the first-order system is effectively indistinguishable from the nonlinear simulation (Ref. 4). The LOES in Fig. 3 is described by:

$$\left(\frac{w}{\theta_0}\right)_{\text{LOES}} = \frac{-0.914}{s + 0.3292} \qquad (9)$$

which yields estimates for the stability derivative $Z_w = -0.3292$ and control derivatives $Z_{\theta_0} = -0.914$, which can be used as initial values of the stability and control derivatives for the full multi-input/multi-output (MIMO) identified models.

The process of simulating a control sweep and identifying frequency responses is repeated for the longitudinal, lateral, and directional inputs, until a complete set of frequency responses is obtained. CIFER® is then used in a MIMO identification of the stability and control derivatives that best matches Eqs. 10 and 11.

$$A_{\text{CIFER}} = \begin{bmatrix} X_u^* & 0 & 0 & 0 & X_q & 0 & 0 & -g \\ 0 & Y_v^* & 0 & Y_p^* & 0 & 0 & g & 0 \\ 0 & 0 & Z_w & 0 & 0 & 0 & 0 & 0 \\ 0 & L_v^* & 0 & L_p^* & 0 & 0 & 0 & 0 \\ M_u^* & 0 & 0 & 0 & M_q & 0 & 0 & 0 \\ 0 & 0 & 0 & 0 & 0 & N_r & 0 & 0 \\ 0 & 0 & 0 & 1 & 0 & 0 & 0 & 0 \\ 0 & 0 & 0 & 0 & 1 & 0 & 0 & 0 \end{bmatrix} \qquad (10)$$

$$B_{\text{CIFER}} = \begin{bmatrix} 0 & 0 & 0 & 0 \\ 0 & 0 & 0 & 0 \\ Z_{\theta_0} & 0 & 0 & 0 \\ 0 & L_{\theta_{1s}}^* & 0 & 0 \\ 0 & 0 & M_{\theta_{1c}} & 0 \\ 0 & 0 & 0 & N_{\theta_{0d}} \\ 0 & 0 & 0 & 0 \\ 0 & 0 & 0 & 0 \end{bmatrix} \qquad (11)$$
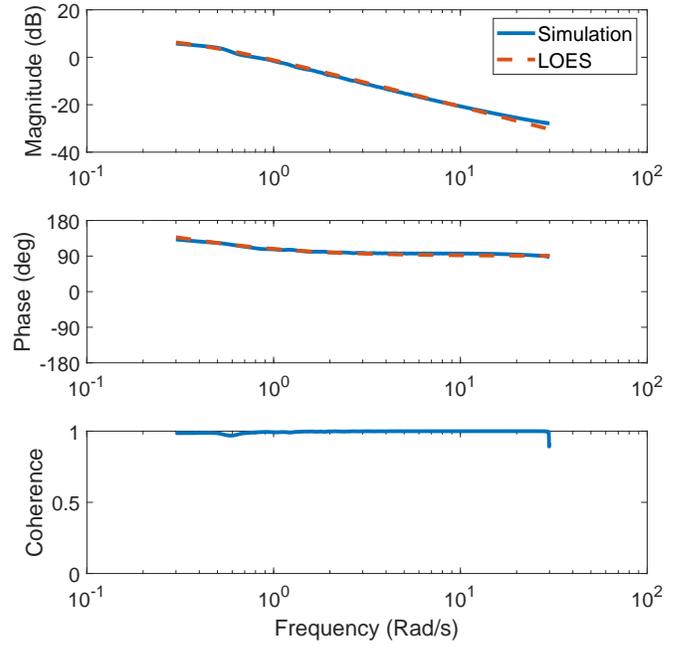
To reduce the number of degrees of freedom, several constraints are introduced to the identification. In particular, based on the symmetry of the vehicle, the longitudinal and lateral dynamics are constrained to be identical (which implies $Y_v = X_u$, $Y_p = -X_q$, $L_v = -M_u$, $L_p = M_q$, and $L_{\theta_{1s}} = M_{\theta_{1c}}$). Additionally, M_u and L_v are obtained using trim data instead of the frequency responses, while X_u is identified from the frequency response u/θ (Ref. 4). Constrained stability derivatives are denoted with a * in Eqs. 10 and 11.

Control System Design

Once a linear model is identified, the control optimization suite CONDUIT® (Ref. 12) is used to optimize a controller that meets ADS-33 handling qualities standards while minimizing actuator effort. The controller is divided into an inner loop, which stabilizes the vehicle and tracks commands in roll/pitch attitude and yaw rate, and an outer loop, which tracks pilot commands in longitudinal, lateral, and vertical velocity. Both inner and outer loops include disturbance rejection specifications. The controller architecture is an explicit model-following (EMF) system (Ref. 12). CONDUIT® is used to tune the feedback gains and the command model frequencies.

The 2-DOF EMF controller, illustrated in Fig. 4 is wrapped around the bare airframe. The input to the mixer includes a feedback signal, with a PID compensator for pitch and roll, and a PI for yaw and velocities, and an inverse model in the feedforward path. Eq. 8 is used as the mixer. The actuator dynamics consists of a rate-limited second-order transfer function based on the UH-60A tail rotor (Ref. 17), which is similar in size to the lifting rotors on the concept quadcopter for the variable-pitch system. For the variable-RPM system, it includes an explicit-model-following feedforward path, and a
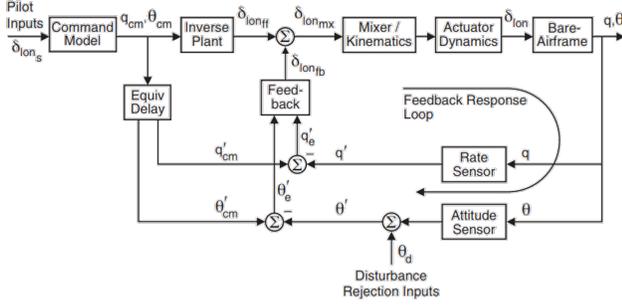
Figure 4: 2DOF Controller Architecture, reproduced from Ref. 12

PI feedback path on the rotor speeds, which determines a voltage input to each motor based on the desired and actual rotor speeds. This introduces the desired motor time constant as a parameter, which can be chosen to minimize the motor inputs, subject to the performance requirements of the inner loop.

The open-loop onset-point (OLOP) is the frequency at which an input (pilot or disturbance) will cause the actuators to reach their rate limits, which can result in pilot-induced oscillations (for piloted inputs) and limit-cycle oscillations (for disturbance inputs). The OLOP specification evaluates the gain and phase of the broken loop transfer function to determine whether the system is prone to such oscillations. For the evaluation of the OLOP specification, a range of 4-36 deg and a maximum actuation rate of 32 °/s (100%/sec) is assumed for the variable-pitch system. For the variable-RPM system, the limitation is assumed to be on the current that is available to any individual motor, which will limit the torque that can be produced and thus, the maximum acceleration achievable by the rotor. If the motor's maximum current limit is K times the current required to hover ($K_t i_{\text{hov}} = Q_A$), then by Eq. 1, the maximum rotor acceleration is given by

$$\dot{\Omega}_{\text{max}} = \frac{K_t K i_{\text{hov}} - Q_{A,\text{hov}}}{I_{\text{rotor}}} = \frac{K_t (K-1) i_{\text{hov}}}{I_{\text{rotor}}} \quad (12)$$

where viscous losses are again assumed to be negligible. By reducing K (and thus $\dot{\Omega}_{\text{max}}$) until the system is unable to meet all of the level 1 requirements, an estimate for the necessary current margin can be obtained. Maximum pilot inputs are taken to be $10°$ in pitch and roll, and $20°/s$ in yaw rate. The maximum disturbance inputs are taken to be $8°$ in roll/pitch attitude and heading. To avoid undesirable oscillations with these input magnitudes, the variable-RPM motors must be capable of receiving 2.5 times the current required to hover, or up to 295A.

RESULTS

System Identification

The identified derivatives, as well as Cramér-Rao bounds and insensitivities are tabulated in Table 2. All of the Cramér-Rao bounds and insensitivities are within the Ref. 4 guidelines, suggesting that the free parameters are uncorrelated and that the frequency responses are sensitive to them.

Table 2: Identified Stability and Control Derivatives

	Pert. Value	ID Value	CR (%)	Insens. (%)
Stability Derivatives				
X_u	-0.0384	-0.0248	——	——
X_q	0.0543	0.0908	1.472	0.860
Z_w	-0.2998	-0.3278	9.722	4.580
M_u	0.0631	0.0557	——	——
M_q	-1.4042	-1.338	2.820	1.108
N_r	-0.1768	-0.1576	17.11	8.384
Control Derivatives				
Z_{θ_0}	-0.8718	-0.9162	2.745	1.293
$M_{\theta_{1c}}$	-1.049	-1.004	1.672	0.6504
$N_{\theta_{0d}}$	0.0439	0.0429	2.676	1.311

Estimates of the model derivatives from a numerical perturbation of the nonlinear model are also included in Table 2. For the most part, the perturbation values are very close to the identified values, indicating that both methods are valid in linearizing the simulation model.

Fig. 5 shows the transfer functions from θ_{1s} to roll rate, p from the identified and numerically perturbed model, overlaid with the frequency response from the nonlinear model. Aside from the gain near the phugoid mode frequency, both the identified and perturbation models capture this frequency response very well, with costs $J_C = 53.71$ (CIFER) and $J_P = 66.76$ (Perturbation), which are acceptable costs (Ref. 4). The largest difference between the linear and nonlinear models is near the phugoid mode frequency, where the coherence is low, indicating significant nonlinear behavior. Within 1/3 and 3 times the design crossover frequency (5 rad/s), the frequency responses essentially coincide with the nonlinear model, making them well-suited to controller design.
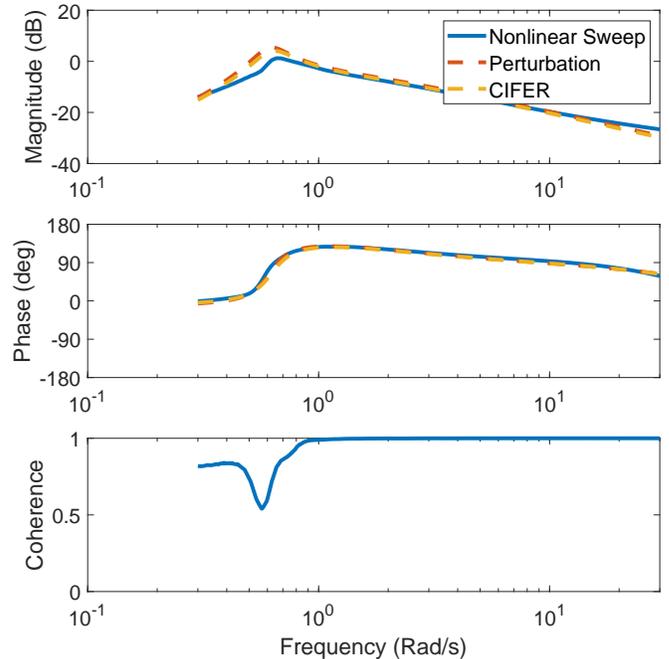

Figure 5: p/θ_{1s} Frequency Responses

(a) Lateral Input

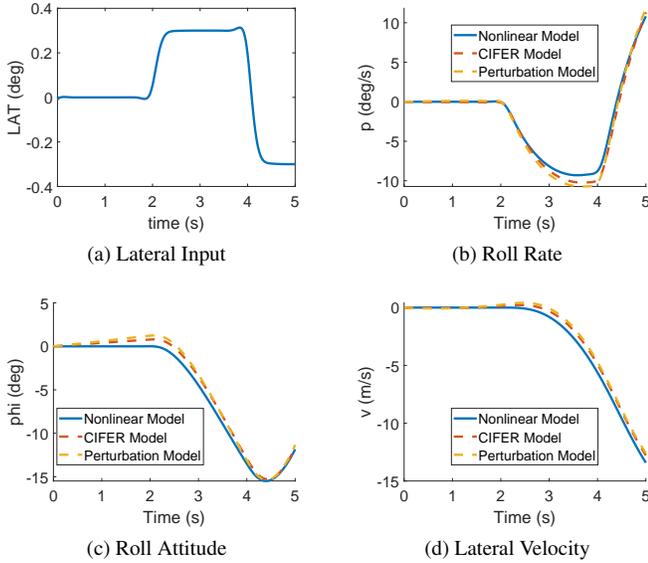(b) Roll Rate

(c) Roll Attitude

(d) Lateral Velocity

Figure 6: Lateral VERIFY Doublet

To confirm that the perturbation and identified models also match the time-response of the vehicle, doublets in all four control inputs are also simulated on the nonlinear model, as well as both linear models. Fig. 6 shows the doublet input in the roll axis, as well as the aircraft response in roll attitude, roll rate, and lateral velocity. Both linear models follow the nonlinear model well, suggesting that both the perturbation method and system identification have good predictive capability. Table 3 shows the J_{RMS} and TIC for the verification doublets in all four axes. $J_{RMS} < 2$, and $TIC < 0.25$, indicating that both the identified model and perturbation model have good predictive accuracy, with the identified model performing somewhat better, as expected (Ref. 4).

Table 3: VERIFY J_{RMS} and TIC

Axis	Identified Model		Perturbation Model	
	J_{RMS}	TIC	J_{RMS}	TIC
Pitch	0.4118	0.0522	0.4780	0.0602
Roll	0.4118	0.0522	0.4731	0.0596
Yaw	0.0379	0.0049	0.0604	0.0078
Heave	0.1650	0.0338	0.0853	0.0178

Control Design

Inner Loop Considering first the variable-pitch system, with an assumption of perfect rotor speed control, as was done in Ref. 10, CONDUIT® is easily able to design a controller that reaches Level 1 in all of the specifications listed in Table 4. More explanation of these specifications is given in (Ref. 12).

If the drive system limitations of Ref. 10 are implemented, CONDUIT® is unable to obtain a set of control gains that can bring the variable-RPM system to Level 1, confirming the conclusions of that paper. However, as the motor time constant is allowed to decrease (thus necessitating greater current capability), CONDUIT® is able to find a controller that

Table 4: CONDUIT® Inner Loop Specifications

Specification	Axes
Hard Constraints	
EigLcG1	All
StbMgG1	Roll, Pitch, Yaw
NicMgG1	Roll, Pitch, Yaw
Soft Constraints	
BnwPiH1	Pitch
BnwRoH1	Roll
BnwYaH1	Yaw
CrsMnG2	Roll, Pitch, Yaw
DrbPiH1	Pitch
DrbRoH1	Roll
DrbYaH1	Yaw
DrpAvH1	Roll, Pitch, Yaw
EigDpG1	All
ModFoG1	All
OlpOpG1 (pilot)	Roll, Pitch, Yaw
OlpOpG1 (disturbance)	Roll, Pitch, Yaw
Summed Objectives	
RmsAcG1 (pilot)	Roll, Pitch, Yaw
RmsAcG1 (disturbance)	Roll, Pitch, Yaw
CrsLnG1	Roll, Pitch, Yaw

reaches Level 1 in all specifications simultaneously. Table 5 shows the optimized handling qualities specifications in roll and yaw (recall that pitch and roll are identical) for both the variable-pitch and variable-RPM systems. In the case of the variable-pitch system in roll, the actuator rate limits are sufficiently large to avoid rate-limiting entirely. The largest motor time constant that allows the vehicle to reach Level 1 is 0.122s, significantly faster than the 0.51s limit imposed by the drive system limits in Ref. 10.

Comparing the variable-RPM system to the variable-pitch system in roll, the presence of the motor dynamics in the variable-RPM vehicle reduces the phase margin and increases phase delay. In yaw, the most notable differences are a small reduction in the phase delay on the variable-RPM system. This occurs because the motor reaction torque does not depend on the rotor speed change, but only on the current, which has been assumed to settle instantaneously. In reality, the electrical dynamics will introduce a small phase delay, but still well within requirements.

Outer Loop (Translational Rate Command) Following the approach of Ref. 12, after optimizing the inner loop, the inner loop gains are frozen, and a translational-rate-command controller was applied to the longitudinal, lateral, and vertical motion of the aircraft. All three axes are constrained to follow a first-order command model. The outer loop specifications used in CONDUIT® are listed in Table 6, with additional explanations of these given in Ref. 12.

Detailed heave axis specifications for the optimized controller on both the variable-RPM and variable-pitch systems are tabulated in Table 7. As was the case with roll, the variable-RPM

Table 5: Inner Loop Handling Qualties Specifications

Parameter	Unit	Roll		Yaw	
		Variable-Pitch	Variable-RPM	Variable-Pitch	Variable-RPM
Stability Gain Margin	dB	11.0	9.36	13.2	6.4
Stability Phase Margin	deg	63.6	49.4	60.0	79.3
Disturbance Rejection Bandwidth (DRB)	rad/s	0.9	0.9	0.72	0.89
Disturbance Rejection Peak (DRP)	dB	3.29	3.28	1.44	0.94
Bandwidth	rad/s	2.5	2.82	1.4	1.68
Phase Delay	s	0.016	0.050	0.016	3.9e-3
Crossover Frequency	rad/s	5	5	5	5
Command Model Following	—	6.02	17.5	0.05	0.87
OLOP Magnitude (Pilot)	dB	N/A	-9.3	2.8	7.0
OLOP Phase (Pilot)	deg	N/A	-180	-118	-84
OLOP Magnitude (Disturbance)	dB	N/A	2.0	2.0	3.4
OLOP Phase (Disturbance)	deg	N/A	-124	-123	-84.0
Actuator RMS (Pilot)	—	5.2e-3	0.08	0.13	0.19
Actuator RMS (Disturbance)	—	0.02	0.26	0.34	0.36

Table 6: CONDUIT® Outer Loop Specs

Specification	Axis
Hard Constraints	
EigLcG1	All
StbMgG1	All
StbMgG1	All
NicMgG1	All
NicMgG1	All
Soft Constraints	
CrsMnG2	All
DrbVxH1	Longitudinal
DrbVyH1	Lateral
DrbVzH1	Heave
DrpAvH1	All
EigDpG1	All
FrqHeH1	Heave
OlpOpG1 (pilot)	All
OlpOpG1 (disturbance)	All
Summed Objectives	
RmsAcG1 (pilot)	All
RmsAcG1 (disturbance)	All
CrsLnG1	All

Table 7: Heave Handling Qualities Specifications

Parameter	Unit	Variable-Pitch	Variable-RPM
Gain Margin	dB	25	24
Phase Margin	deg	92	100
DRB	rad/s	1.03	1.14
DRP	dB	0.67	0.94
Crossover Freq.	rad/s	1	1
Time Delay	s	0.02	0.06
Heave Mode Pole	rad/s	-0.2	-0.2
OLOP Mag. (Pilot)	dB		-1.95
OLOP Phase (Pilot)	deg		-85.8
OLOP Mag. (Dist.)	dB	-20	0.14
OLOP Phase (Dist.)	deg	-143	-79.5
Act. RMS (Pilot)	–	0.078	0.31
Act. RMS (Dist.)	–	0.14	0.33

system has larger delays than the variable-pitch aircraft, and is more susceptible to oscillation due to rate-limiting.

Time Domain Simulations

Vehicle response to a 10° doublet command in roll attitude is shown in Fig. 7. Both the variable-RPM and variable-pitch aircraft follow the commanded signal to about the same degree, which makes sense, as their controllers are designed to the same closed-loop bandwidth. Of particular interest is the current requirement (Fig. 7c), which is about 30 times greater for the variable-RPM system than it is for the variable-pitch system. That the variable-RPM system requires much more

current is no surprise, as the additional torque required to accelerate the rotors is enormous compared to the change in aerodynamic torque associated with small changes in collective pitch.

The vehicle response to a 20°/sec step command in yaw rate is plotted for both aircraft in Fig. 8. Once again, both the variable-pitch and variable-RPM systems follow the first-order command model in r, though there is some deviation in the case of the variable-pitch system. This deviation in yaw rate is due to a rate-saturation that occurs in the pitch actuators, visible in Fig. 8b where the initial response to the step command is a linear increase in θ_{0d}, which causes the aircraft to lag the command model slightly. The yaw-aligned current is plotted in Fig. 8c, which shows that both the variable-pitch and variable-RPM systems require a significantly larger input current to follow a command in yaw rate than in pitch attitude. Further, both aircraft require motor current in excess of 150A when a yaw input is supplied. This is due to the fact that the yaw moment the airframe experiences is the reaction
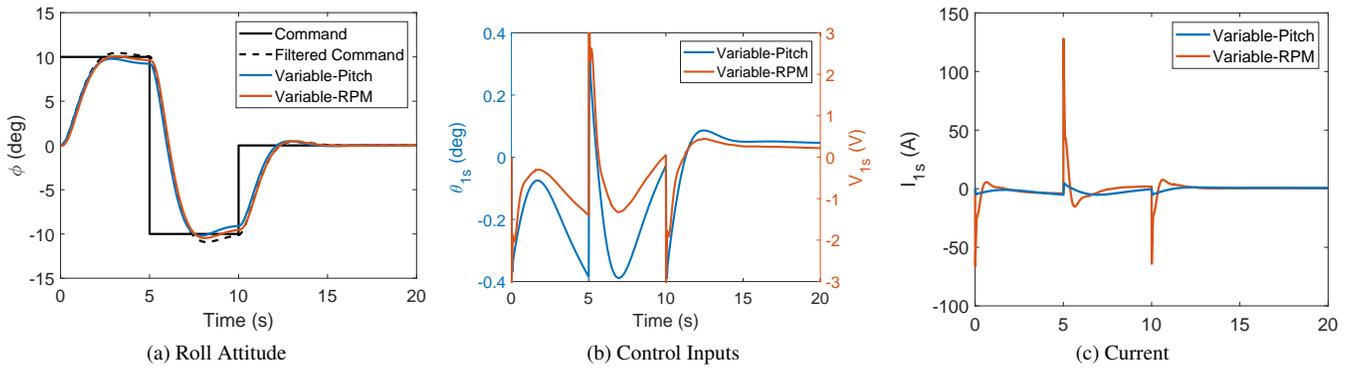
(a) Roll Attitude   (b) Control Inputs   (c) Current

Figure 7: Roll Doublet Response

(a) Yaw Rate   (b) Control Inputs   (c) Current

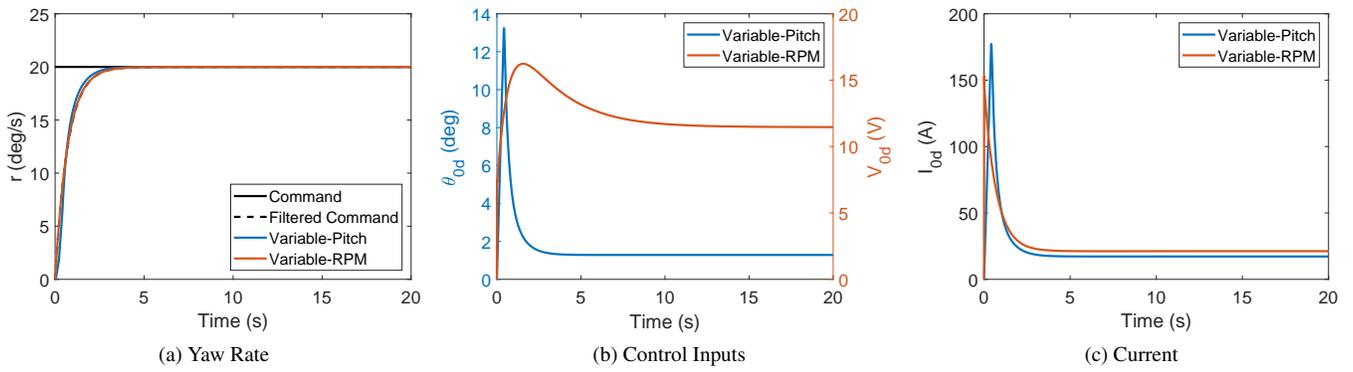Figure 8: Yaw Rate Step

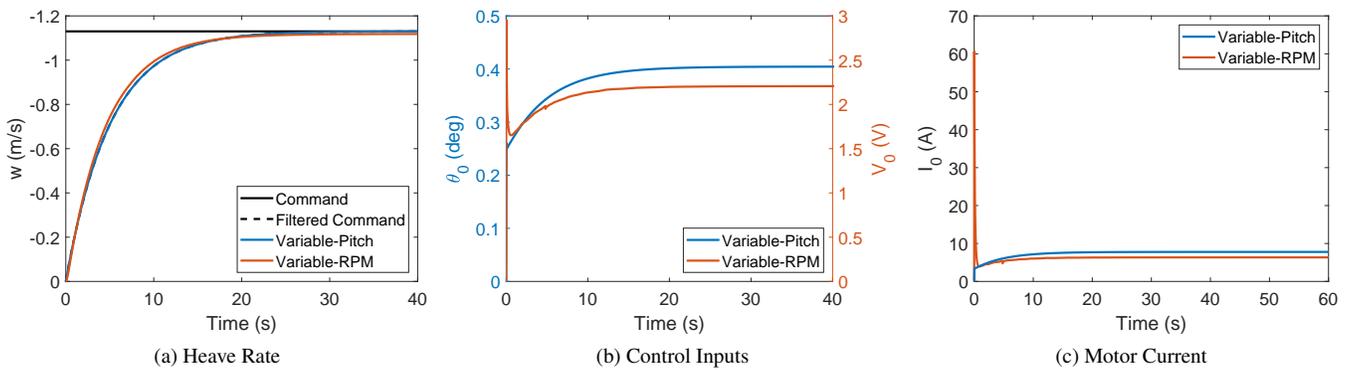(a) Heave Rate   (b) Control Inputs   (c) Motor Current

Figure 9: Heave Step Response

torque from the *motor*, not the aerodynamic torque. Thus, it does not matter if the motor torque is used to overcome increasing aerodynamic torque (in the case of the variable-pitch system) or increase the speed of the rotor (in the case of the variable-RPM aircraft)—the effect on the yaw response of the aircraft is the same. This requirement will appear in any independently-driven rotor system that relies primarily on motor reaction torque to yaw the vehicle.

A climb rate of 1.13 m/s (equal to the 223.1 ft/s specified in Ref. 10) is commanded, with the inputs and vehicle response plotted in Fig. 9. The current requirements (Fig. 9c) are qualitatively different, with the peak current occurring immediately following the step input for the variable-RPM system, and in steady state operation for the variable-pitch system. Ultimately, the variable-RPM system requires up to 60.6 A on each motor, while the variable-pitch system requires only 7.78 A.

Rotor Cant One potential method of circumventing the extreme currents required for yaw control is to cant the rotors in such a way such that differential rotor thrust induces a direct yaw moment in addition to the reaction torque of the motors, as illustrated in Fig. 10, where the blue-colored rotors spin counter-clockwise, and produce a nose-right moment with their thrust and reaction torque.
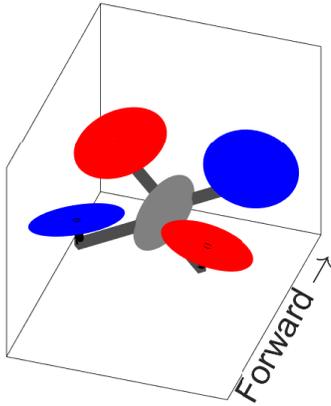

Figure 10: Differential Torsional Cant

The primary effect of differential torsional cant is to increase the sensitivity of yaw moment to differential input (Ref. 18), which is given for the variable-pitch system by

$$N_{\theta_{0d}} = N_{\text{rotors}} \left(\frac{\partial Q_{\text{motor}}}{\partial \theta_{0d}} \cos\gamma + l \frac{\partial T}{\partial \theta_{0d}} \sin\gamma \right) \quad (13)$$

where l is the length of the rotor boom, and γ is the cant angle positive when thrust produces a nose-right moment. Because the RPM is assumed to be governed perfectly on the variable-pitch vehicle, $Q_{\text{motor}} = Q_{\text{aero}}$. Similarly, the variable-RPM system's yaw dynamics include both the direct effect of motor voltage on vehicle moment, and the effect of the changing rotor thrust.

The addition of rotor cant also affects the longitudinal and lateral dynamics significantly, in particular M_u and L_v. If the aircraft is translating forward (positive u), a component of the freestream velocity acts as upwash on the front rotors, and downwash on the rear rotors. This will result in an increase and decrease in thrust, respectively. As a consequence, a nose-up moment is induced on the vehicle, which increases the magnitude of M_u. Conversely, a rightward motion of the vehicle (positive v) induces a right-wing-down moment, which reduces the magnitude of L_v. In the case of the longitudinal dynamics, this further destabilizes the phugoid mode, while the lateral phugoid mode is somewhat stabilized. However, the roll subsidence mode is less stable with less negative L_v, and becomes a divergence mode for sufficiently large γ (if $L_v > 0$). Additionally, the control sensitivity is reduced somewhat, as the component of thrust that acts to produce rolling or pitching moment scales with $\cos\gamma$, though this effect is minor for small γ. The controllers for both systems are re-optimized, using the metrics in Tables 4 and 6 with a rotor cant of 15°

The response of the canted-rotor vehicles to a 20°/sec step command in yaw rate is given in Fig. 11. Both the variable-pitch and variable-RPM systems experience a substantial reduction in the yaw-aligned current compared to the uncanted case. However, the reduction for the variable-pitch system is significantly greater, with a maximum I_{0d} of 22A, compared to the variable-RPM's 89A. This is similar to, though less extreme than, the roll doublet for the uncanted rotor system, as the variable-RPM system must overcome rotor inertia to increase the rotor thrust, while the variable-pitch must only overcome aerodynamic torque. Comparing Fig. 11 to Fig. 8, the introduction of cant reduces the current requirement of the variable-pitch system by about 90%, and the variable-RPM system by about 40%.

The canted vehicles' response to a roll doublet in plotted in Fig. 12. The current required by the variable-RPM quadcopter to follow the doublet is dramatically (about 50%) higher than the uncanted case, due to the change in the lateral dynamics, becoming the limiting case for this vehicle. The current required for the variable-pitch system also increase, though it does not exceed the current required in yaw.

Fig. 13 shows the canted-rotor vehicles accelerating to a climb rate of 1.13 m/s, and the inputs and current required to follow the command model. Due to the redirection of thrust away from the vertical axis, the required current is somewhat greater than for the uncanted case, but heave is not limiting on either vehicle.

DISCUSSION

The weight of an engine is correlated to the peak torque output (proportional to peak current output) by Eq. 14 (Ref. 19).

$$W_{eng} = 0.3928 Q^{0.8587} \quad (14)$$

The peak individual motor torque requirement (and the axis in which that peak is required) is reported for each configuration considered in Table 8. Note that the peak torque includes
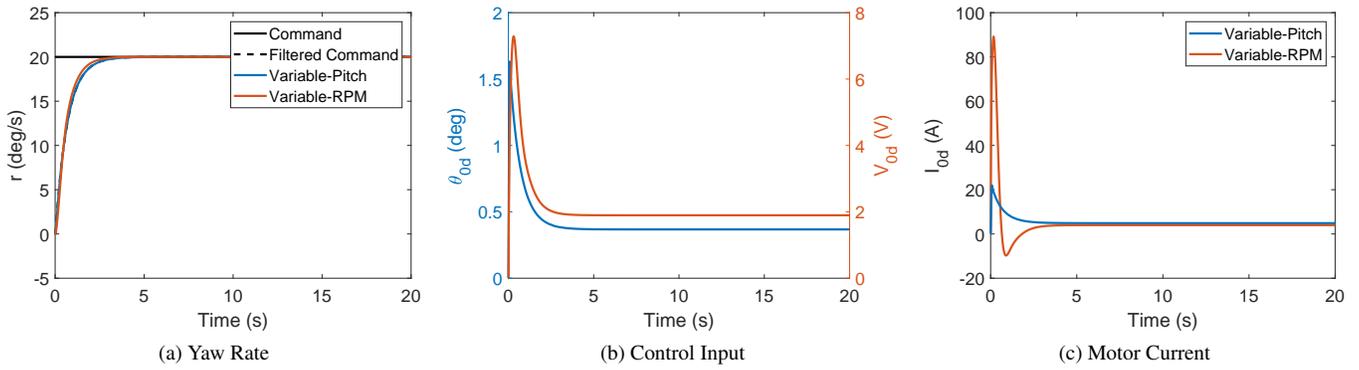
Figure 11: Yaw Step Response with 15° differential torsional cant
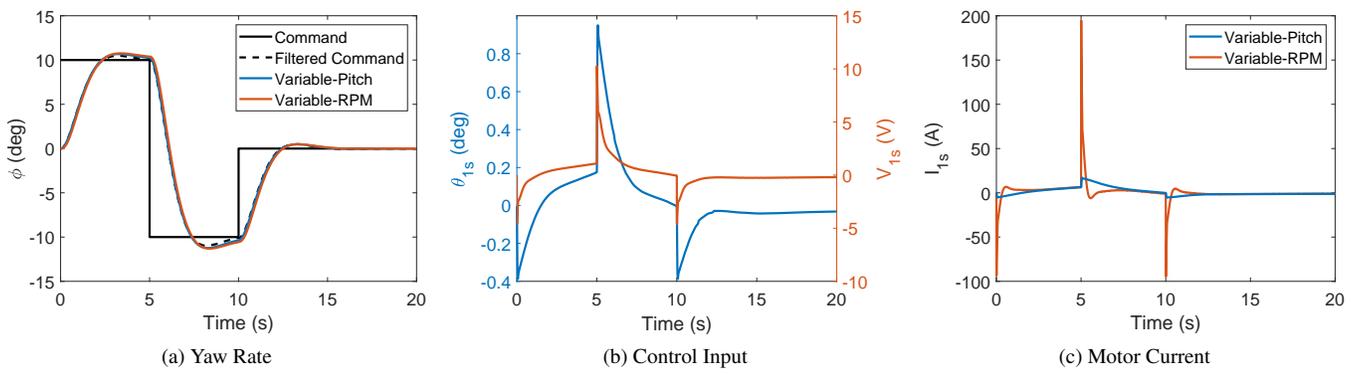

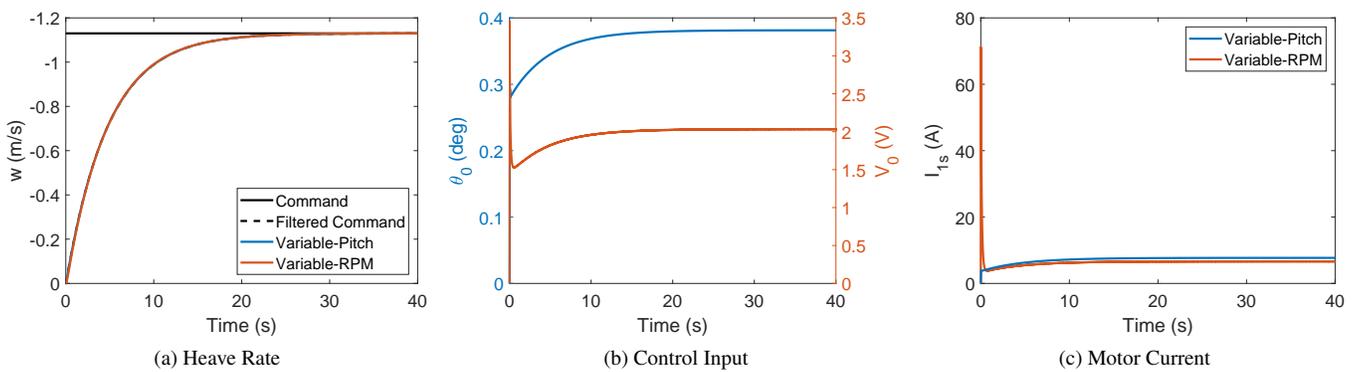Figure 12: Roll Doublet Response with 15° differential torsional cant

Figure 13: Heave Step Response with 15° differential torsional cant

Table 8: Peak Torque and Motor Mass

Control	Configuration	Peak Torque (Nm)	Axis	Motor Mass (kg, each)	Weight Fraction (total)
Variable-Pitch	No Cant	433.4	Yaw	25.2	0.177
	Cant	205.6	Yaw	13.3	0.094
Variable-RPM	No Cant	398.6	Yaw	23.5	0.166
	Cant	374.9	Roll	22.3	0.157

Table 9: Peak Power and Minimum Battery Sizing

Control	Configuration	Peak Power (kW)	Battery Mass (kg)
Variable-Pitch	No Cant	56.7	47.5
	Cant	59.5	49.6
Variable-RPM	No Cant	82.3	68.6
	Cant	87.5	72.9

the torque required to hover. Due to the reliance of zero-cant vehicles on the motor reaction torque to yaw, both the variable-RPM and variable-pitch vehicles require very heavy motors, in total representing 18% and 17% gross weight for the variable-pitch and variable-RPM respectively. The addition of rotor cant helps the variable-pitch system substantially, reducing the peak torque to 205.6 Nm in yaw, corresponding to a motor weight fraction of about 9%.

An additional consideration for the sizing of the electric power system is the power delivery requirements on the batteries. For all of the vehicles considered in this study, the battery requirement will be set by heave motion of the vehicle. Even though heave was not the limiting case for the motor sizing on any of the vehicles, the heave control input is the only control capable of increasing the *net* power required by the vehicle, since on every other axis, the increase in current to one motor occurs simultaneously with an equal reduction in current to another. The peak power requirement, and corresponding minimum battery weight, assuming a maximum burst discharge of 3C and specific energy of 400 Wh/kg (Ref. 13) is tabulated in Table 9. Overall, the minimum battery mass to provide sufficient power represents between 8%-13% of the gross weight of the vehicle, substantially less than the range requirements (21.7% from Ref. 13), suggesting that the specific energy, rather than specific power, is limiting for the concept quadcopter UAM Aircraft.

CONCLUSIONS

1. System identification techniques were used to linearize a nonlinear dynamic simulation of a concept electric quadcopter about a hover condition, and compared to a perturbation model. Both techniques result in linear models that represent the nonlinear simulation very well and offer similar levels of predictive accuracy.

2. CONDUIT®-optimized controllers were obtained for both variable-pitch and variable-RPM variants of the concept quadcopter. To satisfy ADS-33 requirements, the variable-RPM system requires a motor time constant

of less than 0.122s, requiring current well beyond the drive system limits taken in Ref. 10.

3. The current requirements for both direct drive systems to follow closed-loop inputs was dominated by yaw, where the motor reaction torque is used directly to yaw the vehicles. This limitation is associated with the independent nature of the rotors, rather than their control mechanism. The variable-pitch system required significantly less current to follow commanded signals in all axes besides yaw.

4. Rotor cant was then applied to each vehicle, such that rotor thrust worked in concert with the motor torque, in an effort to reduce the current needed to follow yaw commands. The variable-pitch system current requirement was reduced by about 90%, while the variable-RPM system, saw a reduction by only about 40%. The change in the lateral dynamics greatly increased the control effort needed for both vehicles to follow a doublet command in roll, which became the limiting case for the variable-RPM system.

5. Motor and battery weights were compared based on the torque requirements to follow commanded trajectories. The variable-pitch system with cant has the smallest requirement on motor size, only requiring 9% weight fraction dedicated to the motors, representing a 48kg weight savings over the zero-cant variable-pitch vehicle.

ACKNOWLEDGMENTS

REFERENCES

1. Ivler, C., and Tischler, M., "Case Studies of System Identification Modeling for Flight Control Design,"

Journal of the American Helicopter Society, Vol. 58, (1), January 2013, pp. 1–16.

2. Wei, W., Tischler, M. B., and Cohen, K., "System Identification and Controller Optimization of a Quadrotor Unmanned Aerial Vehicle in Hover," *Journal of the American Helicopter Society*, Vol. 62, (4), October 2017, pp. 1–9.

3. Ivler, C., Niemiec, R., Gandhi, F., and Sanders, F. C., "Multirotor Electric Aerial Vehicle Model Validation with Flight Data: Physics-Based and System Identification Models," VFS 75th Annual Forum, Philadelphia, PA, May 13–16, 2019.

4. Tischler, M., and Remple, R., *Aircraft and Rotorcraft System Identification: Engineering Methods with Flight Test Examples*, AIAA Education Series, Reston, VA, 2012.

5. Cheung, K., Wagster, J., Tischler, M., Ivler, C., Berrios, M., Berger, T., Juhasz, O., Tobias, E., Goerzen, C., Barone, P., Sanders, F., Lopez, M., and Lehmann, R., "An Overview of the U.S. Army Aviation Development Directorate Quadrotor Guidance, Navigation, and Control Project," , May 9–11, 2017.

6. "Aeronautical Design Standard, Performance Specification, Handling Qualities Requirements for Military Rotorcraft," Technical Report ADS-33E-PRF, March 2000.

7. Ivler, C., Goerzen, C., Wagster, J., Sanders, F., Cheung, K., and Tischler, M., "Control Design for Tracking of Scaled MTE Trajectories on an IRIS+ Quadcopter," AHS 74th Annual Forum, Phoenix, AZ, May 14–17, 2018.

8. Ivler, C., Rowe, E., Martin, J., Lopez, M., and Tischler, M., "System Identification Guidance For Multirotor Aircraft: Dynamic Scaling and Test Techniques," VFS 75th Annual Forum, Philadelphia, PA, May 13–16, 2019.

9. Walter, A., McKay, M., Niemiec, R., Gandhi, F., and Ivler, C.

10. Malpica, C., and Withrow-Maser, S., "Handling Qualities Analysis of Blade Pitch and Rotor Speed Controlled eVTOL Quadrotor Concepts for Urban Air Mobility," VFS International Powered Lift Conference 2020, San Jose, CA, January 21–23, 2020.

11. Silva, C., Johnson, W., Antcliff, K., and Patterson, M., "VTOL Urban Air Mobility Concept Vehicles for Technology Development," 2018 AIAA AVIATION Forum, Atlanta, GA, June 25–29, 2018.

12. Tischler, M., Berger, T., Ivler, C., Mansur, M., Cheung, K., and Soong, J., *Practical Methods for Aircraft and Rotorcraft Flight Control Design: An Optimization-Based Approach*, AIAA Education Series, Reston, VA, 2017.

13. Johnson, W., Silva, C., and Solis, E., "Concept Vehicles for VTOL Air Taxi Operations," VFS Specialists' Conference on Aeromechanics Design for Transformative Vertical Flight, San Francisco, CA, January 16–19, 2018.

14. Niemiec, R., and Gandhi, F., "Development and Validation of the Rensselaer Multicopter Analysis Code (RMAC): A Physics-Based Comprehensive Modeling Tool," VFS 75th Annual Forum, Philadelphia, PA, May 13–16, 2019.

15. Lopez, M., Tischler, M., Juhasz, O., Gong, A., and Sanders, F., "Development of a Reconfigurable Multicopter Flight Dynamics Model from Flight Data Using System Identification," 8th Biennial Autonomous VTOL Technical Meeting, Mesa, AZ, January 29–31, 2019.

16. Niemiec, R., and Gandhi, F., "Multi-Rotor Coordinate Transforms for Orthogonal Primary and Redundant Control Modes for Regular Hexacopters and Octocopters," 42nd European Rotorcraft Forum, Lille, France, September 5–8, 2016.

17. Ballin, M. G., "Validation of a Real-Time Engineering Simulation of the UH-60A Helicopter," NASA TM 88360, February 1987.

18. Niemiec, R., and Gandhi, F., "Effect of Rotor Cant on Trim and Autonomous Flight Dynamics of a Quadcopter," AHS 74th Annual Forum, Phoenix, AZ, May 14–17, 2018.

19. Johnson, W., "NDARC – NASA Design and Analysis of Rotorcraft," NASA TP 218751, April 2015.